Si(111) strained layers on Ge(111): Evidence for $c(2 \times 4)$ domains

R. Zhachuk,[1,2,*] J. Coutinho,[1] A. Dolbak,[2] V. Cherepanov,[3,4] and B. Voigtländer[3,4]

[1]*Department of Physics & I3N, University of Aveiro, Campus Santiago, 3810-193 Aveiro, Portugal*
[2]*Institute of Semiconductor Physics, Prospekt Lavrentyeva 13, Novosibirsk 630090, Russia*
[3]*Peter Grünberg Institut (PGI-3), Forschungszentrum Jülich, 52425 Jülich, Germany*
[4]*JARA-Fundamentals of Future Information Technology, 52455 Jülich, Germany*

The tensile-strained Si(111) layers grown on top of Ge(111) substrates are studied by combining scanning tunneling microscopy, low-energy electron diffraction, and first-principles calculations. It is shown that the layers exhibit $c(2 \times 4)$ domains, which are separated by domain walls along $\langle \bar{1}10 \rangle$ directions. A model structure for the $c(2 \times 4)$ domains is proposed, which shows low formation energy and good agreement with the experimental data. The results of our calculations suggest that Ge atoms are likely to replace Si atoms with dangling bonds on the surface (rest-atoms and adatoms), thus significantly lowering the surface energy and inducing the formation of domain walls. The experiments and calculations demonstrate that when surface strain changes from compressive to tensile, the (111) reconstruction converts from dimer-adatom-stacking fault-based to adatom-based structures.

I. INTRODUCTION

The importance of stress and strain fields on surface physics is well recognized [1]. They can have a strong impact on surface reconstruction, stability of surface planes, step bunching, and surface diffusion [2–6]. The close chemistry of Si and Ge, combined with a lattice mismatch of about 4%, make the Ge/Si system a prototypical model to study the effect of interfacial elastic strain. Ge epitaxy on Si(111) has been extensively studied and follows the Stranski-Krastanov growth mode [7]. Here, the formation of compressively strained Ge islands on Si(111) substrates has attracted much interest due to their prospective use as template structures in nanoelectronics and nanophotonics [8,9].

First-principles calculations of (111) surface energies of silicon and germanium have predicted a change of the surface structure when the applied elastic strain changes from compressive to tensile [6,10,11]. The surface reconstruction changes from dimer-adatom-stacking fault (DAS) based to adatom based according to the following sequence: 5×5 DAS (strongly compressive) $\rightarrow$ 7×7 DAS (weakly compressive or relaxed) $\rightarrow$ adatom-based reconstructions (relaxed or tensile). A few contenders for adatom-based reconstructions of the (111) surfaces of Si and Ge have been proposed, all showing close surface energy. These are 2×2, $c(2 \times 8)$, $c(2 \times 4)$, and $\sqrt{3} \times \sqrt{3}$, and they were all observed experimentally in Ge/Si(111) [12], with the first three being found on quenched Si(111) surfaces as well [13]. The adatom density in the 2×2, $c(2 \times 8)$, and $c(2 \times 4)$ reconstructions is the same, and these structures differ only in their arrangement. The density of adatoms in the $\sqrt{3} \times \sqrt{3}$ reconstruction is 1/3 higher.

There are several experimental confirmations of the above-mentioned sequence of structural changes. The fully relaxed Ge(111) surface adopts the adatom-based $c(2 \times 8)$ arrangement [14]. Compressively strained Ge layers and islands form during Ge molecular-beam epitaxy (MBE) on Si(111) substrates. In this case, Ge layers with compressive biaxial

strain above $\varepsilon \sim 0.01$ have 5×5 DAS reconstruction, while less strained layers show a 7×7 DAS structure [6]. On the other hand, for Si layers, compressively strained (111) terraces on a stepped Si(111) surface show the tendency to form a 5×5 DAS reconstruction [15], while fully relaxed Si(111) adopts the well-known 7×7 DAS reconstruction [16].

Despite the huge knowledge available for the Ge/Si system, important issues remain to be addressed. For instance, structural data for tensile-strained Si(111) are still missing. Filling in this gap is the main goal of this work, and this is addressed by means of combining first-principles atomistic modeling with scanning tunneling microscopy (STM) and low-energy electron diffraction (LEED) measurements of Si layers grown on Ge(111). We start by reporting the diffraction data, then we move on to the STM data, and finally we describe the results of the calculations, which provide insight into the experimental results.

II. METHODS

A. Experimental procedure

The experiments were performed in two separate ultra-high-vacuum systems, one being equipped with a STM operating at room temperature in constant-current mode and the second one with a LEED system. The STM chamber contains the Si and Ge e-beam evaporators for deposition of Si and Ge by MBE. A Si stripe heated with direct current was used as a source of silicon atoms in the LEED chamber. A quartz crystal balance and STM images were used to measure the deposited amount of Si and Ge. Si was evaporated at a rate of 1 BL/min (BL stands for bilayer). The samples were resistively heated with direct current. The temperature of the substrate was measured using an infrared optical pyrometer.

The clean germanium surface was prepared in the LEED chamber by repeated ion-bombardment cycles of Ar (800 eV), followed by annealing at $800\,^{\circ}$C of Ge(111) samples until a sharp $c(2 \times 8)$ diffraction pattern was observed [Fig. 1(a)]. In the STM chamber, Ge(111) was prepared by MBE growth of three-dimensional (3D) relaxed Ge islands on top of a clean Si(111) surface. Formation details of relaxed Ge islands on Si(111) are given in Refs. [3,4].
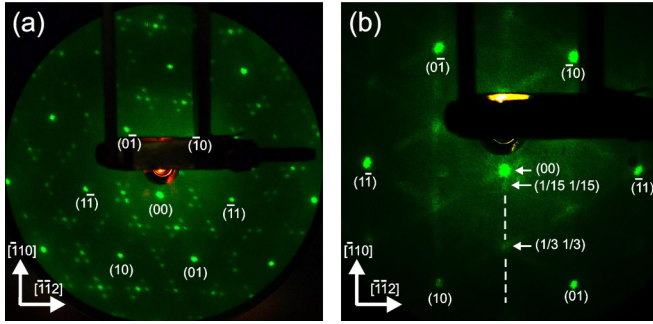
*zhachuk@gmail.com

FIG. 1. (a) LEED pattern from the clean Ge(111)-$c(2 \times 8)$ sample. Electron energy is 90 eV. Integer order spots are marked [23]. (b) LEED pattern from the Ge(111) surface after adsorption of the ~ 4 BL of silicon at $T_{ads} = 550\,°C$. Electron energy is 60 eV. Integer order spots and spots at (1/3 1/3)-like and (1/15 1/15)-like positions are marked. A faint streak along the [$\bar{1}$10] direction is highlighted by a dashed line.

B. Computational details

The surface energy (per unit area) of the reconstructed Si(111) surface is defined and calculated as $\gamma_{rec}(\varepsilon) = \gamma_{1\times1}(\varepsilon) - \triangle\gamma_{rec}(\varepsilon)$, following the procedure detailed in Ref. [6]. Here, $\gamma_{1\times1}(\varepsilon)$ is the energy of the unreconstructed relaxed Si(111)-1×1 surface as a function of applied biaxial tensile strain ε, and $\triangle\gamma_{rec}(\varepsilon)$ is a strain-dependent energy gain due to surface reconstruction. $\gamma_{1\times1}(\varepsilon)$ was calculated using a 12-Si-bilayer-thick symmetric slab according to the following expression:

$$\gamma_{1\times1}(\varepsilon) = \frac{1}{2S_{1\times1}(\varepsilon)}\big[E_{tot}^{1\times1}(\varepsilon) - \mu(\varepsilon)N\big], \quad (1)$$

where μ is the energy per Si atom in bulk under strain (Si chemical potential), $S_{1\times1}$ is the area of a 1×1 surface cell, and $E_{tot}^{1\times1}(\varepsilon)$ is the total energy of the symmetric slab comprising N atoms per simulation cell. Two bilayers in the middle of the slab were kept frozen, while atoms in other layers were allowed to move without any constraints during atomic optimizations.

Each value of $\triangle\gamma_{rec}(\varepsilon)$ was calculated using two 6-bilayer-thick slabs terminated by hydrogen on one side. The first hydrogenated slab had an unreconstructed surface, while the second had a surface reconstruction corresponding to the structure under scrutiny. With this setup, the location of H and Si atoms at the bottom layer was kept frozen during atomic optimizations, while all other atoms were freely allowed to relax. The energy gain per unit area upon reconstruction is therefore

$$\triangle\gamma_{rec}(\varepsilon) = \frac{1}{S_{rec}(\varepsilon)}\big[E_{tot}^{rec-H}(\varepsilon) - E_{tot}^{1\times1-H}(\varepsilon)M - \mu(\varepsilon)K\big], \quad (2)$$

where S_{rec} is the unit cell area of the reconstructed slab, $M = S_{rec}/S_{1\times1}$ is the number of 1×1 reference cells spanned by a reconstructed cell, and K accounts for the number of Si surface atoms in excess of those in the reference cell. In this expression $E_{tot}^{rec-H}(\varepsilon)$ is the total energy of the reconstructed hydrogenated slab, while $E_{tot}^{1\times1-H}(\varepsilon)$ refers to the total energy of the unreconstructed hydrogenated slab with a 1×1 surface cell.

Total energies were calculated from first principles by using the density functional SIESTA code [17]. The exchange-correlation was treated within the local density approximation (LDA) [18]. Test calculations performed using the generalized gradient approximation (GGA) [19] are reported in the Supplemental Material [20] confirming the suitability of LDA to address our problem. The **k**-space integrations over Brillouin zones (BZs) were approximated by sums over Monkhorst-Pack grids of **k** points [21]. Norm-conserving pseudopotentials were employed to account for electronic core states [22], whereas valence states were represented by means of linear combinations of numerical atomic orbitals of the Sankey-Niklewski type, generalized to be arbitrarily complete with the inclusion of multiple ζ orbitals and polarization states [17]. The calculations were performed using double-ζ functions (DZP) basis for Si atoms at the three upper slab layers and single-ζ functions (SZ) for H as well as Si atoms at the remaining layers. Such choice for the basis was previously shown to result in surface energies with comparable accuracy to those using a full DZP basis [6]. Si atoms with DZP basis have two sets of s and p orbitals plus one set of d orbitals. Si atoms with SZ basis have one set of s and p orbitals, while H atoms have a single s orbital.

The unreconstructed bottom surfaces were saturated by hydrogen atoms making 1.50 Å Si-H bonds. The opposite slab surfaces were set up according to specific surface structure models. These are 7×7 DAS [16], as well as single-domain adatom-based 2×2, $c(2 \times 8)$, $c(2 \times 4)$, and $\sqrt{3} \times \sqrt{3}$ reconstructions [14,24]. For the $c(2 \times 4)$ domains, various widths and domain wall structures were considered. Adatoms on 2×2, $c(2 \times 8)$, $c(2 \times 4)$, and $\sqrt{3} \times \sqrt{3}$ surfaces were placed at high-symmetry T_4 adsorption sites.

A uniform real-space grid equivalent to a plane-wave cutoff of 200 Ry was used for Fourier transforming the density and potential fields. The geometry was optimized until all atomic forces became less than 1 meV/Å. Below this threshold, surface structures were considered to have attained equilibrium. All periodic slabs were separated by a 30 Å thick vacuum layer. Under these conditions, converged calculations using a bulk conventional unit cell with a $8 \times 8 \times 8$ BZ-sampling grid gave a lattice constant of Si $a_{Si} = 5.420$ Å. We used specific **k**-point grids for each surface reconstruction/slab, depending on its respective lateral dimensions, namely, $20 \times 20 \times 1$ for 1×1, $3 \times 3 \times 1$ for 7×7 DAS, $10 \times 10 \times 1$ for 2×2, $8 \times 2 \times 1$ for $c(2 \times 8)$ (rectangular surface cell), $12 \times 12 \times 1$ for $\sqrt{3} \times \sqrt{3}$, and $10 \times 12 \times 1$ for single-domain $c(2 \times 4)$. The **k**-point grids for $c(2 \times 4)$ with variable domains were dependent on the domain width: $5 \times 12 \times 1$ for domains comprising 1 adatom in width, $4 \times 12 \times 1$ for domains comprising 2 adatoms, $3 \times 12 \times 1$ for domains comprising 3 adatoms, and $2 \times 12 \times 1$ for domains comprising 4–6 adatoms in width. The resulting **k**-point surface densities in reciprocal space are approximately the same for all cells. Convergence tests regarding the BZ sampling, slab type, and thickness, as well as the basis functions, were reported elsewhere [6].

The constant-current STM images were produced within the Tersoff-Hamann approach [25]. The WSXM software was used to process the experimental and calculated STM images [26].
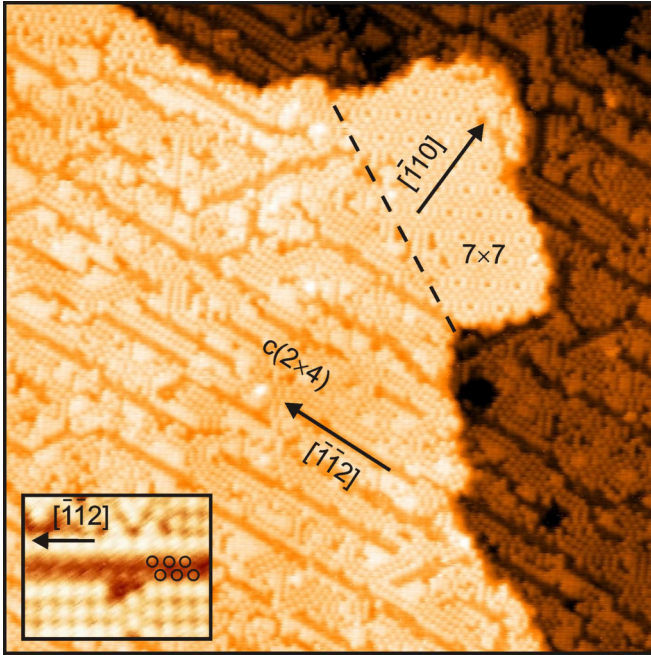
FIG. 2. STM image of the MBE-grown 2 BL silicon on top of a relaxed Ge(111) island, $T_{ads} = 540\,°C$. The image exhibits the 7×7 area and somewhat disordered $c(2 \times 4)$ domains. The dashed line highlights the domain boundary between 7×7 and $c(2 \times 4)$ surfaces. Image size is $640 \times 640\,\text{Å}^2$. $U = +1.8$ V and $I = 1.0$ nA. The inset shows a high-resolution STM image of the DW. The internal zig-zag structure of the DW is highlighted by black circles. The inset dimensions are $71 \times 54\,\text{Å}^2$.

III. RESULTS AND DISCUSSION

A. Experimental STM and LEED results

After cleaning the germanium samples the surface exhibits the well-known $c(2 \times 8)$ diffraction pattern, typical for the clean relaxed Ge(111) surface [see Fig. 1(a)] [27]. The LEED pattern after deposition of 4 BL of silicon on Ge(111) surface at $T_{ads} = 550\,°C$ is shown in Fig. 1(b). Here the spots from the $c(2 \times 8)$ surface reconstruction are completely vanished, and instead the diffraction pattern shows blurred spots at (1/3 1/3)-like positions, faint streaks along $\langle \bar{1}10 \rangle$ directions, and weak spots at about (1/15 1/15)-like positions close to the (0 0) central spot. Similar diffraction patterns were observed for the coverage range $\Theta_{Si} = 2$–4 BL and in the temperature range $T_{ads} = 400$–$550\,°C$. The appearance of the spots at the (1/3 1/3)-like positions after Si MBE growth on Ge(111) surface was also reported in Ref. [28].

A STM image of 2 BL silicon deposited on top of a relaxed 3D Ge island at $T_{ads} = 540\,°C$ is shown in Fig. 2. The image shows two (111) terraces separated by a step. The structure on the terraces shows significant disorder beyond the nanometer scale, but at a smaller scale we can clearly distinguish the existence of predominant patterns. Such observation strongly indicates the existence of several surface reconstructions with close formation energies. Most of the surface is covered with a reconstruction having a rectangular unit cell. This structure looks very similar to the $c(2 \times 4)$ reconstruction found in quenched Si(111) surfaces [13]. The peninsula toward
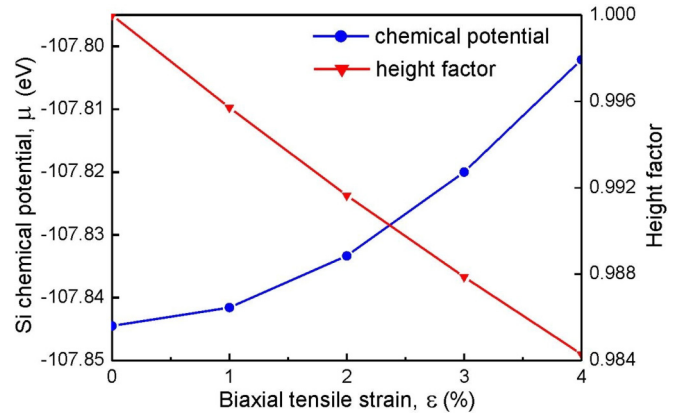

FIG. 3. (Left y axis) Si chemical potential and (right y axis) height factor f_h (see text) for Si(111) interplanar spacing, calculated for different biaxial strain states ε in the (111) plane.

the upper-right corner of Fig. 2 exhibits a 7×7 surface reconstruction, typical of clean relaxed Si(111) surfaces.

The plain $c(2 \times 4)$ reconstruction has a rectangular cell and can form in three rotational domains each rotated by $120°$ as follows from the three-fold C_{3v} symmetry of the (111) substrate. The actual surface structure in Fig. 2 consists of local patches of $c(2 \times 4)$ reconstruction separated by domain walls (DWs) and oriented along the same direction at small scale. The DWs are the dark stripes in Fig. 2 representing surface depressions or trenches. Since the atomic structure of the Si(111)-7×7 reconstruction is known [16], the crystallographic directions in the STM image in Fig. 2 are readily obtained. Thus, it was found that the DWs are elongated along $\langle \bar{1}\bar{1}2 \rangle$ directions. The shorter side of the $c(2 \times 4)$ unit cell is $\sqrt{3}a$ long, where a is the unit length of the unreconstructed (111) surface, and it is parallel to the DW directions. Conversely, the longer side of the $c(2 \times 4)$ unit cell (which is $2a$ long) is perpendicular to the DWs (along $\langle \bar{1}10 \rangle$ directions). The typical $c(2 \times 4)$ domain in Fig. 2 consists of three rows of bright spots (Si adatoms) along $\langle \bar{1}10 \rangle$. The inset in Fig. 2 shows a high-resolution STM image of two $c(2 \times 4)$ patches separated by a DW. The internal structure of the DW is resolved, exhibiting a zig-zag row of dimmed spots highlighted by the small black circles.

B. Theoretical results and comparison with experimental data

Figure 3 shows the calculated silicon chemical potential as a function of (111) biaxial strain in the bulk. From elasticity, it follows that a (111)-biaxially strained cubic solid leads to an opposite strain along [111]. Such effect has to be accounted for in strained surface calculations, and this is done by letting the surfaces freely relax toward the vacuum. In bulk, this effect was considered by using appropriately strained 1×1 bulk slabs with several heights h related to the strain-free height h_0 by a height factor, $f_h = h/h_0$. We determined their equilibrium heights (h values that minimized the energy), which were then used to obtain the energy per Si atom in bulk under strain. Figure 3 also depicts the calculated height factors for Si 1×1 bulk slabs. It shows how the equilibrium distance between (111) layers in bulk depends on the applied biaxial strain.

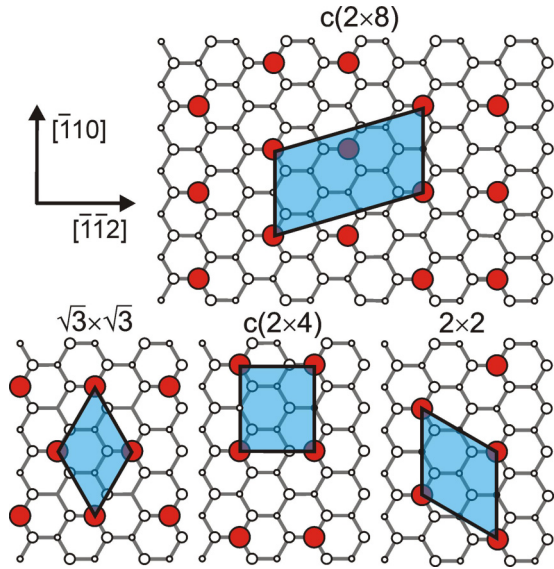FIG. 4. Schematics of adatom-based Si(111) surface reconstructions: $c(2 \times 8)$, $\sqrt{3} \times \sqrt{3}$, $c(2 \times 4)$, and 2×2. A single silicon bilayer with adsorbed silicon atoms is shown. Big and small white-filled circles represent upper and lower atoms of the bilayer, respectively. Large red-filled circles represent Si adatoms. The unit cell for each reconstruction is also outlined.

Several (111) adatom-based reconstructions were considered in this study: 2×2, $c(2 \times 8)$, $c(2 \times 4)$, and $\sqrt{3} \times \sqrt{3}$ (Fig. 4). These are the lowest energy configurations, and therefore the most probable adatom-based (111) reconstructions of Si and Ge. The 2×2, $c(2 \times 8)$, and $c(2 \times 4)$ reconstructions were observed on clean quenched surfaces of Si(111) and at Ge/Si(111) growth [12,13]. The formation of the $\sqrt{3} \times \sqrt{3}$ surface reconstruction was observed on MBE-grown Ge/Si(111) as reported in Refs. [6,24].

Figure 5 shows the calculated surface energies γ_{rec} of Si(111) as a function of applied tensile strain ε for various experimentally observed reconstructions. In agreement with
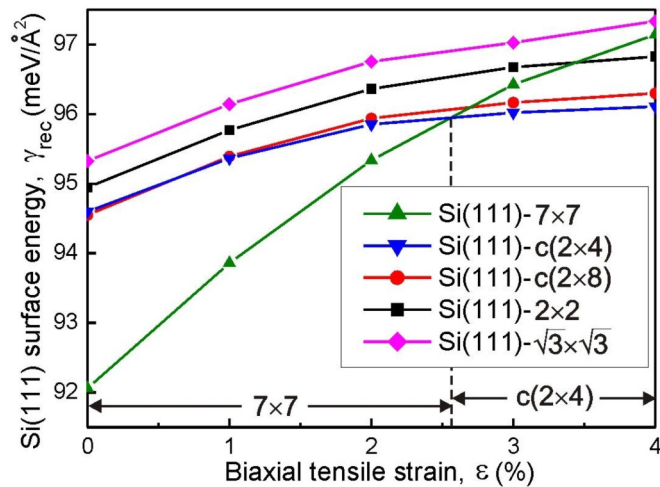

FIG. 5. Si(111) surface formation energies calculated for tensile biaxial strain states in the range $\varepsilon = 0\%$–4% for 7×7, $c(2 \times 8)$, $\sqrt{3} \times \sqrt{3}$, $c(2 \times 4)$, and 2×2 surface reconstructions.
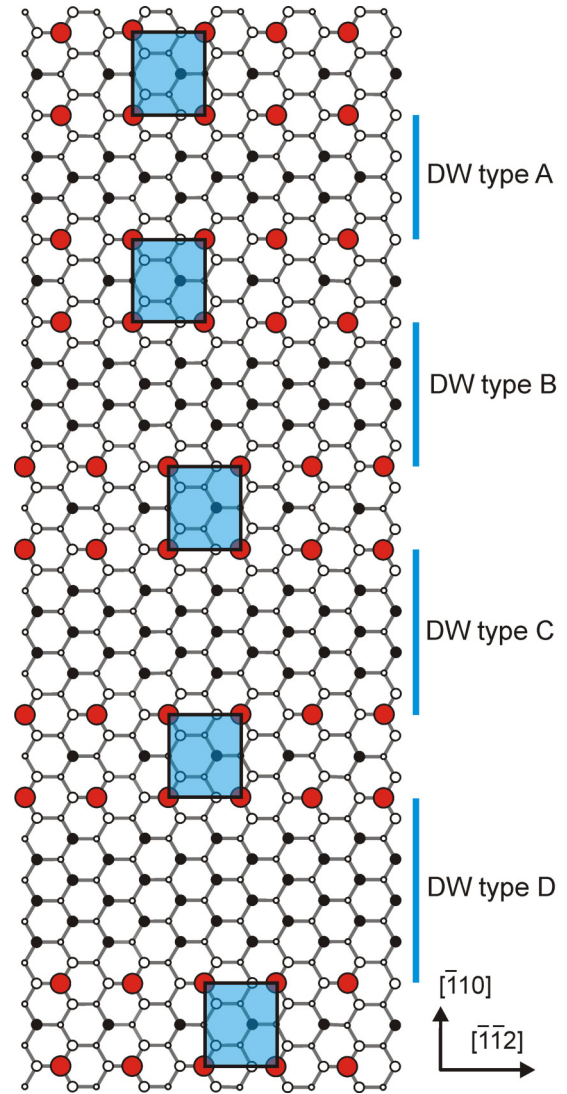

FIG. 6. Schematics of possible DW atomic structures, from type A to type D. Big white-filled circles represent upper atoms of the bilayer with all bonds saturated; black-filled circles represent upper atoms of the bilayer with one dangling bond (rest-atoms); small white-filled circles represent lower atoms of the bilayer; large red-filled circles represent Si adatoms. The $c(2 \times 4)$ unit cell is outlined on each domain.

previous studies, we find that adatom-based structures are more stable than 7×7 DAS-based structures when the biaxial tensile strain above $\sim$2.5% is applied to Si(111) [6,10,11]. As opposed to the simple adatom-based reconstructions, the presence of several reconstruction elements (dimers, adatoms and stacking faults) in DAS-based surfaces make these intrinsically compressive [6]. Hence, with increasing the surface tensile strain, the surface formation energy of DAS-based reconstructions grows faster than that of adatom-based structures. As one can see from Fig. 5, the lowest energy reconstruction at $\varepsilon \gtrsim 2.5\%$ is $c(2 \times 4)$. This result explains the STM observations depicted in Fig. 2.

Four contenders for the DW atomic structures that separate neighboring $c(2 \times 4)$ domains were investigated and are represented in Fig. 6. The proposed DW models are simply
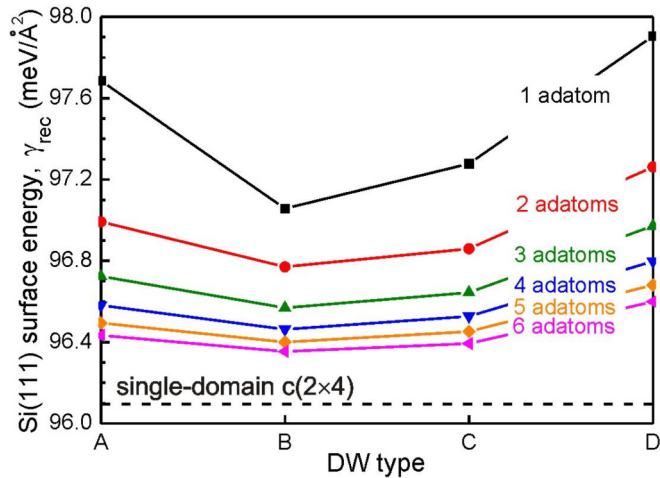
FIG. 7. Si(111)-$c(2 \times 4)$ surface formation energies calculated for 4% tensile biaxial strain, as a function of the DW width [corresponding to four different $c(2 \times 4)$ DW structures, A–D]. Each plot corresponds to a specific $c(2 \times 4)$ domain width measured in number of adatoms between neighboring DWs.
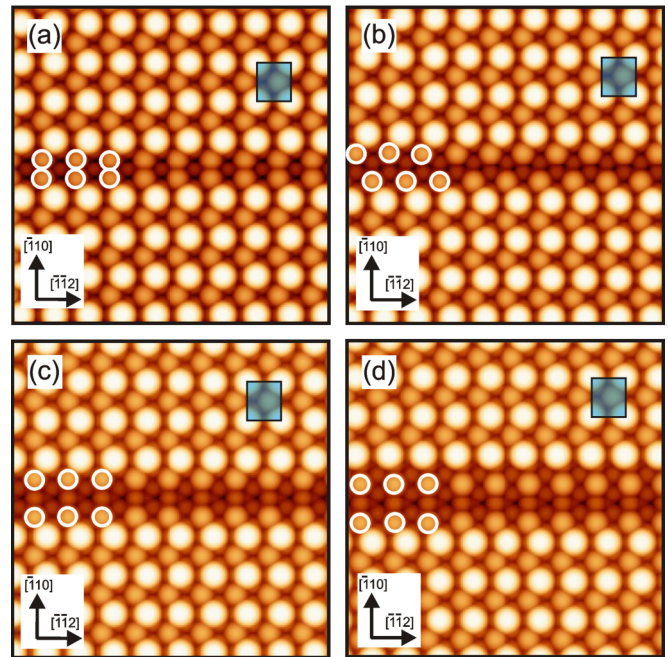

FIG. 8. Calculated STM images of four different types of DWs structures: (a) DW type A, (b) DW type B, (c) DW type C, and (d) DW type D. Bias voltage corresponds to +1.0 eV with respect to the theoretical Fermi level. The $c(2 \times 4)$ unit cells are outlined. The structure of DWs is highlighted by white circles.

bare (111) substrate areas with increasing width (types A–D). The width of these DWs is in approximate agreement with the experimental STM image in Fig. 2. For the sake of space saving, the width of the $c(2 \times 4)$ domains as represented in Fig. 6 is limited to two Si atomic rows. The surface combining the Si(111)-$c(2 \times 4)$ domains with DWs was simulated using periodic boundary conditions, keeping the domain width fixed, but considering variable-width DW models (as shown in Fig. 6).

Figure 7 shows that irrespective of the domain width, the Si(111)-$c(2 \times 4)$ surface with DW type B shows the lowest formation energy and therefore is expected to correspond to the observations. The calculated STM images of the Si(111)-$c(2 \times 4)$ surface near the DW area (DW types A–D) are presented in Figs. 8(a)–8(d), respectively. The DW internal structure exhibits relatively bright spots, somewhat dimmed as compared to those of Si adatoms. Some of these spots are highlighted by white circles. Similar spots are also observed within the $c(2 \times 4)$ domains, between Si adatoms. All these spots are due to substrate rest-atoms raised after slab relaxation. As shown in Fig. 8(b), only DW type B is compatible with the experimentally observed zig-zag structure as depicted in the inset of Fig. 2. This corroborates the assignment of the DW structure to type B based on its low surface energy. It is noteworthy that DW type D (shown in Fig. 6), spanning six parallel rows of rest-atoms, is *a priori* expected to show a zig-zag pattern in STM due to rows 1 and 6 edging the $c(2 \times 4)$ domains. Instead, we found that in the ground state, spots from parallel rows 2 and 6 (or 1 and 5) are "switched on", adding further support to our assignment of type B structure to the observed DWs.

We can conjecture that the reason behind the appearance of DWs is the partial relaxation of the silicon layers under tensile strain. Accordingly, the observed domain and DW widths must be governed by a balance between the energy gain from surface strain relief and the energy penalty due to formation of unsaturated bonds across the bare surface area of

the DWs. Figure 2 suggests that the crossing point involving these two factors takes place for a domain width equivalent to about 3 adatoms. Still, the observed surface structure should correspond to an energy state below that of single-domain $c(2 \times 4)$ reconstruction (without DWs), and that is not what Fig. 7 shows. In fact, the calculated data suggest that DWs should not appear in strained Si(111) under thermodynamic equilibrium conditions. Figure 7 shows that despite having been grown at relatively high temperatures, and therefore likely to be close to thermodynamic equilibrium, the domains with 3 adatoms width are metastable by ~ 0.5 meV/Å^2 (with respect to a full covered $c(2 \times 4)$ surface). We also note that the $c(2 \times 4)$ domains were observed in rather thin (2–4 BL thick) Si layers, so that the number of atomic layers used in calculations should be appropriate to describe the strain within the slab.

Until now, we have missed an ingredient in calculations which can, in principle, play a relevant role in DW formation. That is Si/Ge intermixing. Unfortunately, the chemical resemblance between Si and Ge prevents their discrimination on the surface by using STM imagery like that shown in Fig. 2. Surface termination with bismuth allows us to distinguish between Si and Ge atoms [29,30], but that would alter the surface reconstruction. The (111)-7×7 reconstructed "peninsula" in Fig. 2 may suggest that the surface consists of clean silicon layers, where strain is released through the surrounding step edges. Clean Ge(111) layers, which can also form 7×7 reconstruction under compressive strain [6], can be ruled out due to the absence of compressive strain in the surface. Yet, we cannot exclude the formation of a Si-rich SiGe(111)-7×7 reconstruction.

In order to understand how Si/Ge intermixing can change the surface energy and its structure, we performed a set of exploratory calculations [31]. Accordingly, we used Si/Ge(111) hydrogenated slabs, where both Si and Ge atoms had DZP basis set. The first (reference) slab had 3 BL of pure Si on top of 3 BL of pure Ge. In the second slab, we kept the same Si/Ge layered structure, but one atom at the topmost Ge layer (at the Si/Ge interface) was replaced by Si, while one Si atom at the surface was replaced by Ge. The calculated energy differences show that the exchange of Si and Ge atoms leads to an energy drop of up to 0.4 eV per atom pair. We suggest that most energy gain comes from the less reactive Ge dangling bond (when compared to that of Si) when Ge occupies rest-atom or adatom sites, both at the $c(2 \times 4)$ domain and at the DW surfaces. Surface sites with saturated bonds show less energy gain or no gain at all.

Next, we constructed a $c(2 \times 4)$ slab with domain width equivalent to 3 adatoms and DW type B, where *all* atoms with dangling bonds at the Si surface were replaced by Ge. Concurrently, an equal number of Ge atoms at the topmost layer of Ge (at the Si/Ge interface) were replaced by Si. This Ge-terminated surface shows an energy gain of 14.2 meV/$\mathring{A}^2$ with respect to the reference slab (with no Si/Ge intermixing). The single-domain $c(2 \times 4)$ reconstruction without DWs shows a 1 meV/$\mathring{A}^2$ lower energy gain. This difference is naturally explained by the two times higher density of dangling bonds in the DW area as compared to that in the $c(2 \times 4)$ domains. Hence, the impact of Si/Ge intermixing on the surface energy is more pronounced in the DW area. Combining surface energies calculated for strained Si(111) layers (Fig. 7) with energy gains due to Si/Ge intermixing, we estimate surface energies of single-domain $c(2 \times 4)$ and $c(2 \times 4)$ with DWs (3 adatoms width) as 82.9 meV/$\mathring{A}^2$ and 82.4 meV/$\mathring{A}^2$, respectively. This makes the formation of DWs energetically favorable when Si/Ge intermixing is taken into account. Auger electron spectroscopy or photoelectron spectroscopy measurements could help to determine if silicon layers are actually terminated by Ge atoms.

The calculated LEED patterns representing fast Fourier transforms of calculated STM images are shown in Fig. 9. Figure 9(a) shows the calculated diffraction pattern from single-domain $c(2 \times 4)$ reconstruction without DWs, where only one rotational domain is present. Figure 9(b) shows a diffraction pattern from the three possible rotational domains of $c(2 \times 4)$ reconstruction (still without DWs). The calculated LEED patterns in Figs. 9(a) and 9(b) cannot account for the experimental LEED pattern shown in Fig. 1(b). We clearly have to consider the effect of DWs on the LEED patterns.

Figure 9(c) shows the calculated diffraction pattern from one rotational domain of $c(2 \times 4)$ reconstruction with type-B DWs. A domain width equivalent to 3 adatoms was considered. The translational unit cell for the surface with DWs includes few $c(2 \times 4)$ cells and is not rectangular [32]. One can see that the spots from the $c(2 \times 4)$ reconstruction are now split along the [$\bar{1}$10] direction (perpendicular to the DW orientation). This is the effect of intensity modulation by DWs. The resulting reciprocal unit cell is smaller than that of the $c(2 \times 4)$ reconstruction without DWs, and consequently it is not rectangular as well. The influence of surface defects
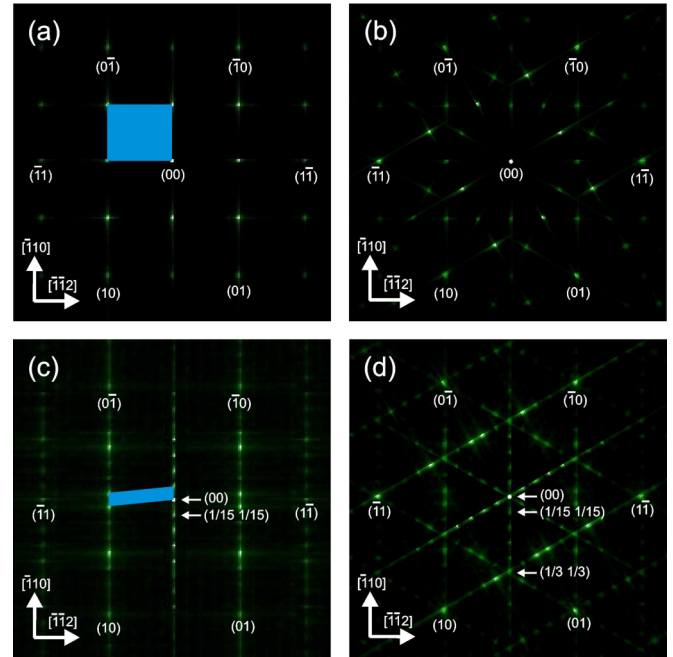

FIG. 9. Calculated LEED patterns. (a) Single-domain $c(2 \times 4)$ reconstruction (no DWs). (b) Three rotational domains (no DWs). (c) $c(2 \times 4)$ domains with 3 adatoms width (one rotational domain) separated by DWs type B. (d) $c(2 \times 4)$ domains with 3 adatoms width (three rotational domains) separated by DWs type B. Reciprocal unit cells are outlined in (a) and (c). See Supplemental Material for the simulated STM images used to compute the LEED patterns in (a) and (c) [34].

(including DWs) on LEED patterns was extensively studied in the past (see, for instance, Ref. [33] and references therein). The split size (δ) is inversely proportional to the periodicity of $c(2 \times 4)$ domains (Γ) in the direction perpendicular to DWs:

$$\Gamma = w_{\mathrm{D}} + w_{\mathrm{DW}} = \frac{100\%}{\delta\%} \times a_{\mathrm{Ge(111)}} \sin 60^{\circ}, \qquad (3)$$

where 100% of the surface BZ corresponds to the distance between the (0 0) spot and integer first-order spots, while $a_{\mathrm{Ge(111)}}$ is the lattice constant of the unreconstructed Ge(111)-1×1 surface. w_{D} and w_{DW} stand for domain and DW widths, respectively. Thus, combining Eq. (3) with the experimental LEED pattern in Fig. 1(b) we may estimate the *macroscopic* average domain width [33].

Figure 9(d) shows the calculated diffraction pattern from all three rotational domains of $c(2 \times 4)$ reconstruction with DW type B. The pattern shows many similarities with the experimental LEED results shown in Fig. 1(b). The split size in Fig. 9(d) is about 7% which is equivalent to the (1/15 1/15)-like spots visible in Fig. 1(b). From the LEED data, we obtain an average $c(2 \times 4)$ domain width equivalent to 3 adatoms, which fits nicely to the STM results. All six (1/15 1/15)-like spots with similar intensity are visible around the (0 0) spot in Fig. 1(b). Therefore, each $c(2 \times 4)$ rotational domain occupies similar surface areas. Only first-order (1/15 1/15) fractional spots are visible in experimental LEED pattern in Fig. 1(b), while higher-order spots are smeared out and become weak streaks along $\langle \bar{1}10 \rangle$-like directions. The intersections of these

streaks give rise to (1/3 1/3)-like spots with weak intensity. The suppression of higher order fractional spots in diffraction patterns is due to irregular widths of $c(2 \times 4)$ domains. A similar effect was observed, for example, on LEED patterns of nickel-contaminated Si(100) containing irregular 2×1 domains [35,36].

IV. CONCLUSIONS

Tensile-strained Si(111) prepared by silicon MBE growth on Ge(111) substrates and on relaxed Ge(111) template structures on top of 3D islands was studied by low-energy electron diffraction, scanning tunneling microscopy, and first-principles calculations. We show that the calculated Si(111) surface reconstructions and their respective energy ordering as a function of strain match the experimental observations. Namely, it is shown that under tensile strain the Si(111) surface exhibits domains of adatom-based $c(2 \times 4)$ reconstruction, separated by domain walls. This contrasts with the relaxed

and compressive strain regimes where dimer-adatom-stacking fault structures are seen. An atomic model for the domain wall that separates neighboring $c(2 \times 4)$ domains is proposed, showing low surface energy and good agreement with the experimental microscopy and diffraction data. The average domain width is also reported. According to the calculations, the formation of domain walls on a pure Si(111) surface always implies an energy penalty, suggesting that their appearance is unfavorable under thermodynamic equilibrium conditions. We suggest that Ge/Si intermixing can stabilize the DWs, hence explaining this apparent contradiction.

[1] P. Müller and A. Saúl, Surf. Sci. Rep. **54**, 157 (2004).

[2] J. Tersoff, Y. H. Phang, Z. Zhang, and M. G. Lagally, Phys. Rev. Lett. **75**, 2730 (1995).

[3] V. Cherepanov and B. Voigtländer, Appl. Phys. Lett. **81**, 4745 (2002).

[4] V. Cherepanov and B. Voigtländer, Phys. Rev. B **69**, 125331 (2004).

[5] L. Persichetti, A. Sgarlata, G. Mattoni, M. Fanfoni, and A. Balzarotti, Phys. Rev. B **85**, 195314 (2012).

[6] R. Zhachuk, S. Teys, and J. Coutinho, J. Chem. Phys. **138**, 224702 (2013).

[7] B. Voigtländer, Surf. Sci. Rep. **43**, 127 (2001).

[8] J. Liu, R. Camacho-Aguilera, J. T. Bessette, X. Sun, X. Wang, Y. Cai, L. C. Kimerling, and J. Michel, Thin Solid Films **520**, 3354 (2012).

[9] K. A. Lozovoy, A. V. Voytsekhovskiy, A. P. Kokhanenko, V. G. Satdarov, O. P. Pchelyakov, and A. I. Nikiforov, Opto-Electron. Rev. **22**, 171 (2014).

[10] D. Vanderbilt, Phys. Rev. B **36**, 6209 (1987).

[11] J. J. L. Mercer and M. Y. Chou, Phys. Rev. B **48**, 5374 (1993).

[12] U. Köhler, O. Jusko, G. Pietsch, B. Müller, and M. Henzler, Surf. Sci. **248**, 321 (1991).

[13] M. Koike, Y. Einaga, H. Hirayama, and K. Takayanagi, Phys. Rev. B **55**, 15444 (1997).

[14] R. S. Becker, B. S. Swartzentruber, J. S. Vickers, and T. Klitsner, Phys. Rev. B **39**, 1633 (1989).

[15] M. K. Kim, D.-H. Oh, J. Baik, C. Jeon, I. Song, J. H. Nam, S. H. Woo, C.-Y. Park, and J. R. Ahn, Phys. Rev. B **81**, 085312 (2010).

[16] K. Takayanagi, Y. Tanishiro, S. Takahashi, and M. Takahashi, Surf. Sci. **164**, 367 (1985).

[17] J. M. Soler, E. Artacho, J. D. Gale, A. García, J. Junquera, P. Ordejón, and D. Sánchez-Portal, J. Phys.: Condens. Matter **14**, 2745 (2002).

[18] J. P. Perdew and A. Zunger, Phys. Rev. B **23**, 5048 (1981).

[19] J. P. Perdew, K. Burke, and M. Ernzerhof, Phys. Rev. Lett. **77**, 3865 (1996).

[20] See Table 1 in Supplemental Material at http://link.aps.org/supplemental/10.1103/PhysRevB.96.085401 for energy gains due to various Si(111) surface reconstructions for LDA and GGA.

[21] H. J. Monkhorst and J. D. Pack, Phys. Rev. B **13**, 5188 (1976).

[22] N. Troullier and J. L. Martins, Phys. Rev. B **43**, 1993 (1991).

[23] See Fig. 1 in Supplemental Material at http://link.aps.org/supplemental/10.1103/PhysRevB.96.085401 for a schematics of the Ge(111)-$c(2 \times 8)$ diffraction pattern and marking of the fractional order spots.

[24] Z. H. Qin, D. X. Shi, H. F. Ma, H.-J. Gao, A. S. Rao, S. Wang, and S. T. Pantelides, Phys. Rev. B **75**, 085313 (2007).

[25] J. Tersoff and D. R. Hamann, Phys. Rev. B **31**, 805 (1985).

[26] I. Horcas, R. Fernández, J. M. Gómez-Rodríguez, J. Colchero, J. Gómez-Herrero, and A. M. Baro, Rev. Sci. Instrum. **78**, 013705 (2007).

[27] I. Razado-Colombo, J. He, H. M. Zhang, G. V. Hansson, and R. I. G. Uhrberg, Phys. Rev. B **79**, 205410 (2009).

[28] T. Ichikawa and S. Ino, Surf. Sci. **136**, 267 (1984).

[29] J. Myslíveček, F. Dvořák, A. Stróżecka, and B. Voigtländer, Phys. Rev. B **81**, 245427 (2010).

[30] R. Zhachuk and J. Coutinho, Phys. Rev. B **84**, 193405 (2011).

[31] See Fig. 2 in Supplemental Material at http://link.aps.org/supplemental/10.1103/PhysRevB.96.085401 for the structural models used to calculate Si/Ge intermixing and corresponding surface energies.

[32] See Fig. 2(b) in Supplemental Material at http://link.aps.org/supplemental/10.1103/PhysRevB.96.085401 for the translational unit cell of the surface with DWs.

[33] M. Henzler, Appl. Surf. Sci. **11-12**, 450 (1982).

[34] See Fig. 2 in Supplemental Material at http://link.aps.org/supplemental/10.1103/PhysRevB.96.085401 for the simulated STM images used to compute the LEED patterns in Figs. 9(a) and 9(c).

[35] A. E. Dolbak, B. Z. Olshanetsky, S. I. Stenin, and S. A. Teys, Surf. Sci. **218**, 37 (1989).

[36] H. Neddermeyer, Rep. Prog. Phys. **59**, 701 (1996).